

Forward and Inverse Design of Kirigami via Supervised Autoencoder

Paul Z. Hanakata,¹ Ekin D. Cubuk,² David K. Campbell,³ and Harold S. Park⁴

¹*Department of Physics, Harvard University, Cambridge, Massachusetts 02138, USA**

²*Google Brain, Mountain View, California 94043, USA*

³*Department of Physics, Boston University, Boston, Massachusetts 02215, USA*

⁴*Department of Mechanical Engineering, Boston University, Boston, Massachusetts 02215, USA*

(Dated: August 13, 2020)

Machine learning (ML) methods have recently been used as forward solvers to predict the mechanical properties of composite materials. Here, we use a supervised-autoencoder (sAE) to perform inverse design of graphene kirigami, where predicting the ultimate stress or strain under tensile loading is known to be difficult due to nonlinear effects arising from the out-of-plane buckling. Unlike the standard autoencoder, our sAE is able not only to reconstruct cut configurations but also to predict mechanical properties of graphene kirigami and classify the kirigami with either parallel or orthogonal cuts. By interpolating in the latent space of kirigami structures, the sAE is able to generate novel designs that mix parallel *and* orthogonal cuts, despite being trained independently on parallel or orthogonal cuts. Our method allows us to both identify novel designs and predict, with reasonable accuracy, their mechanical properties, which is crucial for expanding the search space for materials design.

INTRODUCTION

Recently, there has been growing interest in investigating the nonlinear mechanics of perforated thin sheets across length scales ranging from the macroscale [1–4] down to nanoscale systems [5–8]. The cuts in a thin sheet—known as kirigami cuts—induce buckling and other motions (e.g. rotations). These mechanisms result in new properties, such as enhanced ductility [7] and auxeticity [9] that are different from the pristine (cut-free) counterpart. This simple strategy has led to programable kirigami actuators which are the building blocks of soft-robots [1, 10]. While many analytic descriptions have been developed to understand the changes in mechanical behavior due to the cuts [1, 2, 4], these analytic approaches are used to describe systems with repeating and uniform cut patterns or to optimize a specific target property. An analytical model that can describe how the mechanical properties of kirigami sheets depend on the interaction of *different* types of cuts has not been developed.

For the *inverse design* problem, one ongoing challenge for kirigami structures is in designing them to achieve specific properties. Most current ML techniques rely on applying ML to select top candidates from a *fixed* library [8, 11, 12]. The usual approach is to perform “active learning” where the model is trained incrementally with data proposed by the ML [8, 11], or by training the model with a significant amount of data to predict top candidates [12]. For both approaches, ML (the “forward solver”) must be applied to the *entire* library. Even when the computational cost of the ML approach is much lower than the ground truth data generator (physics-based simulations or experimental data), in a highly complex system with many degrees of freedom, it is not practical to use ML to calculate the properties of all candidates to

find the best candidates.

In computer vision problems, *generative models* have shown to be successful in generating realistic synthetic samples [13]. Unlike supervised learning, the generative models are trained to capture an underlying data distribution and to learn important features. For instance, variational autoencoders have been used to capture the important information from a high dimensional space of the real representation (e.g. image) within a lower dimensional space, known as the *latent space*. The latent vectors capture important features, for instance smiles in facial images, and thus can be used for interpolation which is useful for generating new synthetic samples.

In optimizing material properties, we often have some key observable properties, such as ultimate stress and fracture strain. The goal is to make the learned hidden (latent) variables correlated to the key properties, so that we can perform optimization in the *latent space*, which has a significantly reduced dimensionality compared to that of the discrete (original) representation of the structures. This strategy gives a large advantage over performing optimization in the original representation space, and has recently been applied for designing materials with a large design space, such as drugs, organic molecules, and optical metamaterials [14–17].

In this paper we propose a *supervised autoencoder* (sAE) for inverse structural design. We set up our training such that we can evaluate the effectiveness of interpolation (generating new designs) within and outside the training domain. First, we find that the sAE is able to generate designs consisting of mixed cuts even though the sAE is trained with kirigami structures with only parallel and orthogonal cuts, which shows the ability of sAE to perform interpolation in the latent space. Moreover, in the latent space, the sAE captures similarities and differences between distinct structures with different cut types

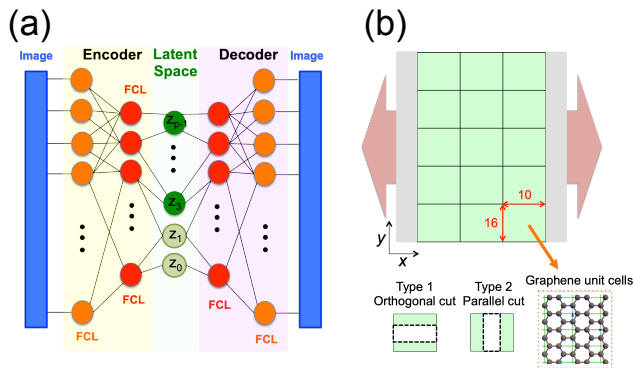


FIG. 1. (a) Schematic of an autoencoder. (b) Schematic of graphene kirigami partitioned into 3×5 grids. The training set contains either parallel or orthogonal cuts (no mixing of cut types). Each grid consists of 10×16 graphene unit cells. Kirigami is stretched in the x -direction by moving the edges (grey regions).

whereas the information about cut types is not provided during the training. As generalization requires diversity in the training set, we can leverage the ability of the sAE to distinguish different structures in the latent space to use it as an exploration strategy to propose designs that lie outside the training data.

SUPERVISED AUTOENCODER

An autoencoder (AE) consists of two parts: (i) an encoder \mathcal{E} that maps a vector to a reduced representation and (ii) a decoder \mathcal{D} that reconstructs a vector to its original representation from the reduced representation. Let $\mathbf{x} \in \mathbb{R}^n = \mathcal{X}$ be the n -dimensional vector, and $\mathbf{z} = (z_0, z_1, \dots, z_{p-1}) \in \mathbb{R}^p = \mathcal{Z}$ be the p -dimensional latent variables. Since the goal is to have a compressed representation, p is chosen to be smaller than n . Mathematically we can write this transformation as, $\mathcal{E} : \mathcal{X} \rightarrow \mathcal{Z}$, $\mathcal{D} : \mathcal{Z} \rightarrow \mathcal{X}$. In the standard AE the mean reconstruction loss is given by,

$$\mathcal{L}^{\mathcal{X}}(\mathbf{x}, \mathbf{x}') = \frac{1}{m} \sum_{i=1}^m |\mathbf{x}^{(i)} - \mathbf{x}'^{(i)}|^2 = \frac{1}{m} \sum_{i=1}^m |\mathbf{x}^{(i)} - \mathcal{E}(\mathcal{D}(\mathbf{x}^{(i)}))|^2, \quad (1)$$

where i is the i th data point and m is the number of training samples. AEs are widely used for unsupervised learning where only unlabelled data \mathbf{x} are provided. In many physical systems, we want to include the known properties to the unsupervised AE such that the supervised AE (sAE) learns new “hidden” features. In this work, we choose p to be 10 and we enforce the first two latent vectors (z_1 and z_0) to learn ultimate (maximum) stress σ^u and the corresponding ultimate strain ϵ^u . We choose a latent dimension that is larger than the number of known properties since kirigami with different cuts can

have the same mechanical properties (e.g. due to symmetries). Thus, for this proposed supervised AE (sAE) architecture, we introduce a target property mean squared error loss function,

$$\mathcal{L}^{\mathcal{Y}}(\mathbf{y}, \mathbf{z}) = \frac{1}{m} \sum_{i=1}^m |\mathbf{z}^i - \mathbf{y}^{(i)}|^2 = \frac{1}{m} \sum_{i=1}^m \sum_{k=0}^{d-1} |z_k^i - y_k^{(i)}|^2, \quad (2)$$

where $\mathbf{y} \in \mathbb{R}^d = \mathcal{Y}$ is a d -dimensional vector that contains the known properties and d equals to the number of observable properties. The total loss function then becomes $\mathcal{L} = \mathcal{L}^{\mathcal{X}} + \eta \mathcal{L}^{\mathcal{Y}}$, where η is a hyperparameter. We found that $\eta = 1$ is a reasonable choice to get a good accuracy without training the model for too long. We standardize \mathbf{y} to have zero mean and unit standard deviation [18], which is essential for training a neural network as the optimizer treats all directions uniformly in the parameter space [19, 20].

In this work, we used the typical AE architecture [?], where a schematic of the sAE is shown in Fig. 1(a). For the encoder, we use a deep neural network (DNN) architecture similar to our previous work [8] with one additional fully-connected (FCL) layer. The decoder consists of two fully-connected layers. More details of the DNN architecture and training procedure can be found in the supplemental information (SI).

Results—We train the sAE with configurations having parallel cuts, i.e. that are parallel to the loading direction (x -axis), and orthogonal cuts (y -axis), as shown in Fig. 1(b). Each orthogonal cut has a size of 3×16 unit cells (holes), whereas each parallel cut has a size of 3×10 unit cells (holes). We trained the sAE with configurations having between 0 and 15 cuts. Each graphene membrane has 2400 unit cells and we define the density ρ as the number of holes divided by the total number of unit cells. This gives a range of density from 1 (0 cuts) to 0.7 (15 cuts or equivalently 720 holes) [21]. We used LAMMPS (Large-scale Atomic/Molecular Massively Parallel Simulator) to simulate graphene kirigami under tension [22]. The molecular dynamics (MD) simulation procedure is similar to our previous work [8] and the simulation details can be found in the SI. The sAE takes an image of size 2400 (30×80) and outputs an image with the same size. While we train the sAE with configurations having large cuts (~ 30 holes in each grid), in principle, the sAE can generate configurations with any arbitrary cut size, i.e. as small as one hole. We simulated all possible configurations of parallel and orthogonal cuts *without* mixing the two types. As we allow either only 0-15 orthogonal cuts or 0-15 parallel cuts, we obtain a total of 62,558 configurations, of which 29,791 are non-detached configurations with orthogonal cuts while the remaining are the configurations with parallel cuts which have non-detached configurations. The networks were trained with 50% of the data set while the remainder of the data set is used for validation and test set (25% each).

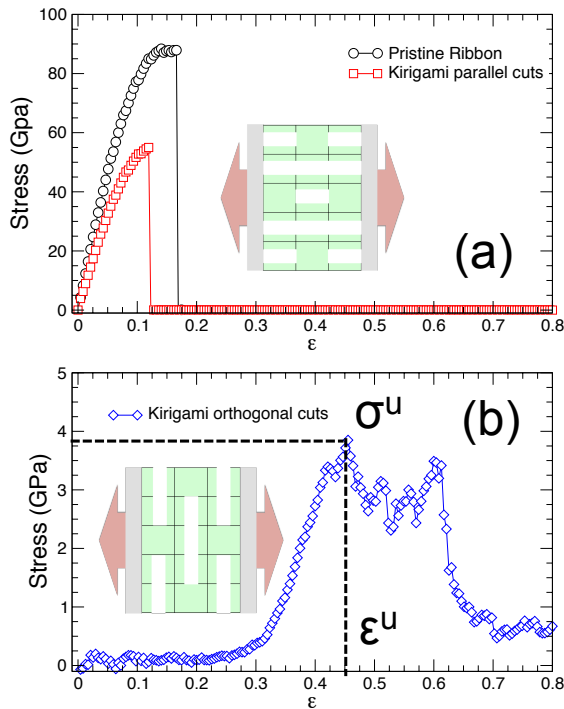


FIG. 2. Stress as a function of strain for pristine graphene ribbon and kirigami with parallel cuts (a) and kirigami with orthogonal cuts (b). The stress-strain curve changes significantly as the orientation of the cuts is changed.

We first show that the mechanical properties of cut graphene are indeed highly dependent on the material architecture. In some composite designs, the stiffness of materials can be well-described by density. In contrast for kirigami, the nonlinear regime becomes important and thus predicting properties beyond the linear regime, such as ultimate stress and yield strain, via density is no longer viable [4, 7, 8]. For instance in typical kirigami geometries, the effective stiffness in the post-buckling regime is proportional to bending rigidity as opposed to the Young’s modulus [4, 23].

Thus, the *architecture* of the materials strongly impacts their properties. To demonstrate this, in Fig. 2(a) and (b), we plot stress-strain curves of kirigami with parallel and orthogonal cuts. Importantly, the orthogonal cuts in Fig. 2(b) represents the same cut pattern with the same number of cuts as shown for the parallel cut kirigami in Fig. 2(a). As can be seen, simply changing the orientation of each cut but fixing the cut configurations results in a completely different stress-strain curve, consistent with MD simulations by Ref. [24]. Furthermore, we can see from Fig. 3(a) that density alone does not correlate to σ^u or ϵ^u . This further suggests that the desired global properties are highly dependent on the structural configuration.

To summarize, the mechanical properties of graphene kirigami depend not only on (i) material density but also on (ii) cut configurations, and on (iii) cut orientations. We will show that despite this complexity our sAE is able to organize the materials based on the structural properties that are not encoded to the latent space in a supervised fashion.

Next, we investigate the learned latent variables. We first turn off the constraint \mathcal{L}^Y ($\eta = 0$) to enable the AE to learn in an unsupervised manner. To better visualize the 10D latent space we project the latent vectors to a 2D space using principal component analysis (PCA). The latent vectors are generated by passing \mathbf{x} of the training data through the encoder. From Fig. 3 we see that the 2D projected latent variables (from the training data) clearly separate the two different cut orientations despite the fact that the AE was not provided with the cut orientations. In addition to separating structures based on cut orientation, the AE clusters different structures based on their density. This is similar to how a latent variable found by AE coincides with the net magnetization (the order parameter) in the Ising spin system [25]. However, none of the latent variables found by the AE strongly correlates to either σ^u or ϵ^u in this kirigami problem.

We now include the property predictions into the latent space. Similar to the unsupervised AE, as shown in Fig. 3 the sAE clusters the data based on cut orientation. Furthermore, by color coding the data by the normalized ultimate strain $\bar{\epsilon}^u$, and normalized ultimate stress $\bar{\sigma}^u$, we see that in each phase the sAE organizes structures based on their properties. This shows that the sAE has not only learned to distinguish different structures of the input image in the real representation but also to predict their mechanical properties. We use the R^2 metric to quantify the performance of the model in predicting $\bar{\epsilon}^u$ and $\bar{\sigma}^u$ as we did in our previous work [8]. The R^2 on the training, validation, test sets for σ^u (ϵ^u) are 0.99 (0.92), 0.99 (0.87) and 0.99 (0.87), respectively. Thus we indeed find that z_0 and z_1 are correlated to the normalized ϵ^u and σ^u , respectively. Similarly, the sAE is successful in reconstructing the structures \mathbf{x} in the real space. We use the fraction of correctly placed graphene unit cells as an accuracy metric and we obtain accuracies of 99.4% for training, validation, and test set. Details regarding the distribution of all latent variables and the reconstructed structures of the can be found in the SI. For the remainder of the paper we will focus on the sAE.

GENERATING NEW DESIGNS VIA INTERPOLATION IN THE LATENT SPACE

While the sAE can be used to generate designs by sampling from the latent space, the question remains as to how the latent values (z s) are set as they all reside in the same space and are interconnected. Another sim-

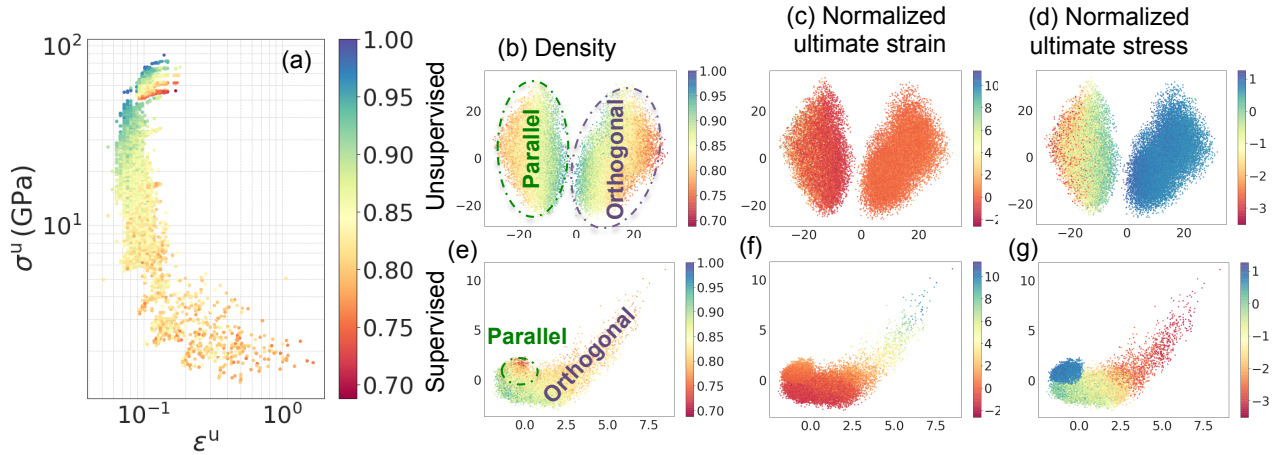


FIG. 3. (a) Log-log plot of ultimate stress as a function of ultimate strain for *all* simulated data. The colorbar represents the density, where density alone does not correlate with ultimate strain. Projected latent space for (b)-(d) unsupervised autoencoder and (e)-(g) supervised autoencoder. The two axis are found by PCA. The unsupervised autoencoder is able to distinguish different structures based on their cut density and cut orientations. The supervised autoencoder successfully captures not only the structural differences but also mechanical properties such as normalized ultimate strain and normalized ultimate stress.

ple approach is to perform interpolation in the latent space. In this section, we introduce metrics to quantify novel designs and show that we can generate new designs while simultaneously predicting their mechanical properties with reasonable accuracy. The question we want to address here is what objective function should be chosen in order to generate new kirigami designs that were not in the training data.

In a p -dimensional space, we can write $\mathbf{z} = (z_0, z_1, \dots, z_{p-1})$ in terms of a radius r and $p - 1$ angles $(\phi_0, \phi_1, \dots, \phi_{p-2})$. By analogy to a genetic algorithm, new designs (children) can be generated by combining two parents and applying a mutation rule. This approach is usually performed in the real representation of the genome. In the current work, we generate new designs from the *latent space*, which is much smaller than the real space. The simplest approach to generate new designs is by performing linear interpolation between two latent vectors. Here, we use *spherical linear interpolation* (SLERP), which has been used for interpolating images in generative networks [26, 27]. Suppose we have two parent vectors $\mathbf{v}_\alpha, \mathbf{v}_\beta \in \mathcal{Z}$, then a new vector can be generated $\mathbf{v}_t = \frac{\sin[(1-t)\Omega_{\alpha\beta}]}{\sin\Omega_{\alpha\beta}}\mathbf{v}_\alpha + \frac{\sin[t\Omega_{\alpha\beta}]}{\sin\Omega_{\alpha\beta}}\mathbf{v}_\beta$, where $0 \leq t \leq 1$ and $\Omega_{\alpha\beta} = \cos^{-1} \frac{\mathbf{v}_\alpha \cdot \mathbf{v}_\beta}{|\mathbf{v}_\alpha||\mathbf{v}_\beta|}$. With this approach the interpolated design lies on the surface of p -dimensional sphere, and the interpolated vector can then be decoded into a real structure.

As our goal is to perform inverse design outside the training domain, an important step is to quantify similarity. We use angular distance (Ω_{tk}), and Tanimoto distance (T_{tk}) to quantify the difference between the in-

terpolated structure and the parent structure:

$$\Omega_{tk} = \cos^{-1} \frac{\mathbf{v}_t \cdot \mathbf{v}_k}{|\mathbf{v}_t||\mathbf{v}_k|} / \Omega_{\alpha\beta} \quad (3)$$

$$T_{tk} = \frac{\mathbf{X}_t \cdot \mathbf{X}_k}{|\mathbf{X}_t|^2 + |\mathbf{X}_k|^2 - \mathbf{X}_t \cdot \mathbf{X}_k}, \quad (4)$$

where t is the interpolation step and $k = \alpha, \beta$. Note that $\Omega_{tk} \sim 0$ indicates two structures that are close in latent space whereas $T_{tk} \sim 1$ indicate structures that are close in real space.

We generated a total of 200 new structures from 10 pairs of random configurations obtained from the training dataset. Each interpolation path contains 20 intermediate structures. We then pass the structures through the encoder and compare the predicted mechanical properties with the MD results. The mechanical predictions of half of the 200 new structures are within 15% error relative (in real units) to the MD results. Our discussion will focus on a few representative examples. Details on how configurations were randomly selected and results on all other structures can be found in the SI.

Fig. 4(a) shows intermediate structures from interpolating two structures with orthogonal cuts (path 3) and orthogonal and parallel cuts (path 5 and path 8). Fig. 4(b) shows the corresponding property predictions and the MD results (path 3 and path 8) in the normalized ultimate stress vs ultimate strain plot (mechanical space). As shown in Fig. 4(a)(p3), the interpolation scheme allows us to generate similar structures in regions that are close to the training domain. It can be seen the MD results are close to the predicted values.

In contrast, as shown in Fig. 4(a) (p5) and (p8), by interpolating two configurations that have different cut

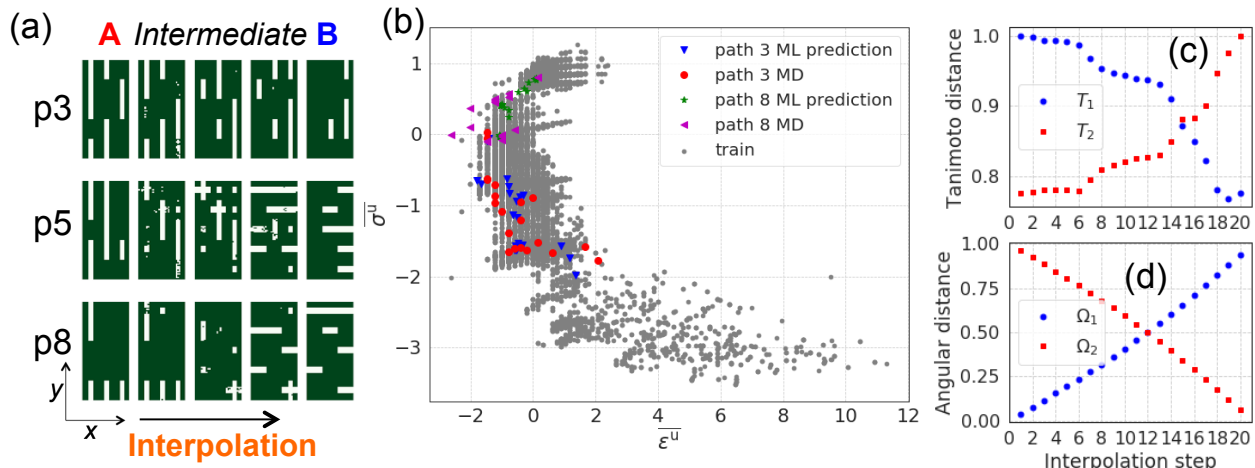


FIG. 4. (a) Three representative new designs generated by interpolating from parent A (first column) to parent B (last column). Some structures with mixed cuts are obtained when the two parent structures have distinct cut types. (b) Comparison between ML predictions and MD results plotted in the normalized ultimate stress vs normalized strain plot (mechanical space). Similarity metrics for path 8 measured by (c) Tanimoto distance and (d) angular distance. Note that the kirigami are stretched in the x -direction and the edges are not shown.

types, we are able to generate designs consisting of separate parallel and orthogonal cuts as well as overlapping (mixed) cuts, whereas the training dataset does not have configurations with two types of cuts. Because the sAE is interpolating two structures that are mechanically and structurally different (*far* in the mechanical space), the predicted mechanical properties are not exact but still in reasonable agreement. The mean absolute ultimate strain relative error of the three representative structures are 8.5%, 51%, and 15% for p3, p5, and p8, respectively. The mean absolute ultimate stress relative error of the three representative structures are 10%, 43%, and 11% for p3, p5, and p8, respectively. Several works in computer vision have also shown that ML models do not generalize well to samples that are from a slightly different distribution than the training set [28–30], which means that the ML model can capture only a subset of the underlying physics. Comparison between MD and ML predictions for all structures can be found in the SI.

In Figs. 4(c) and (d) we plot the similarity metrics for path 8. We found that designs that are different in real space are not necessarily different in the latent space [31]. For instance in path 8, there are many distinct designs with similar mechanical properties. By comparing the visualization of the structures and their mechanical properties to the similarity metrics, we find that the angular distance performs best in capturing *both* the differences in structures and mechanical properties.

With this in mind, we recommend using the angular distance as a novel metric to guide searching in the latent space and to generate new diverse training data sets or potential designs to obtain non-redundant models. To

show how we can utilize our approach to search novel designs, we compare two search strategies in generating structures: (i) select the structure with the highest strain or (ii) select structure that is the most different, as measured by the angular distance similarity metric. Out of the 200 representative generated designs, we obtained 87 designs with mixed cuts when we used strategy (ii) whereas we only obtained four designs with mixed cuts when we used strategy (i) (see Figs. 8 and 9 in the SI). It is an open question in ML research how to best maximize search diversity, which we hope to further investigate in future studies.

CONCLUSIONS

In this work, we have demonstrated the ability of the supervised autoencoder (sAE) to perform both forward and inverse design of graphene kirigami. With regards to forward design, by distinguishing the difference in mechanical properties depending on the cut pattern and orientation, the sAE can overcome the traditional problem of needing to search through the entire design space library to obtain novel designs. With regards to inverse design, the sAE enables the generation of structures by passing the latent variables to the decoder. Because the latent space is significantly smaller than the real space, we can perform optimization in the latent space as has previously been done to discover new drugs and chemical compounds [15]. Most importantly, we are able to classify designs that are different from the training data by measuring similarity metrics. While the mechanical property

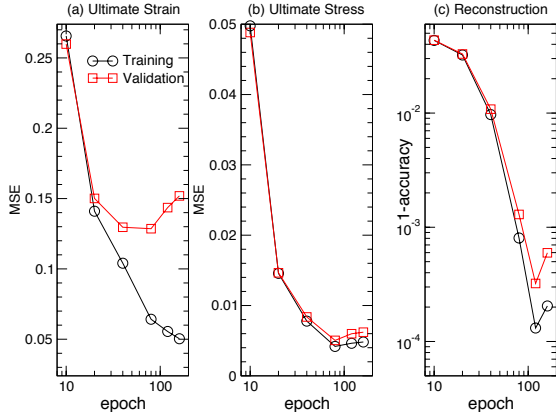


FIG. 5. Plot of mean squared error (MSE) of (a) normalized ultimate strain, (b) normalized ultimate stress, and (c) reconstruction loss [$1 - \text{accuracy}$] as a function of epoch number.

predictions of the sAE for structures that are significantly different (far from the training data) are less accurate, the sAE can still be utilized to propose novel designs. As online databases for mechanical systems, such as the mechanical MNIST database [32], are developed, our model will be important for learning the underlying physics in a reduced-dimensional space, as well as for proposing novel designs. Moreover, as the local structures are tightly connected to electronic properties, this method can be extended for learning electronic properties in 2D materials, such as pseudomagnetic and electric polarization, as a function of defects or kirigami cut patterns [33–38].

P. Z. H. developed the codes and machine learning methods, performed the simulations and data analysis, and wrote the manuscript with input from all authors. P.Z.H. acknowledges support from the National Science Foundation through Grant No. DMR-1608501 and via the Harvard Materials Science and Engineering Center through Grant No. DMR-1420570. P. Z. H., D. K. C. and H. S. P. acknowledge the Boston University High Performance Shared Computing Cluster. P. Z. H. is grateful for the Hariri Graduate Fellowship. P. Z. H. thank David R. Nelson for helpful discussions.

SUPPLEMENTAL INFORMATION

Molecular Dynamics

We used LAMMPS (Large-scale Atomic/Molecular Massively Parallel Simulator) to simulate graphene kirigami under tension [22]. The carbon-carbon interactions are described by the AIREBO potential [39], where the simulation procedure is similar to our previ-

ous work [8]. The lattice constants of the rectangular graphene unit cell are $\sim 4.2 \text{ \AA}$ and 2.4 \AA along the x and y directions, respectively. The graphene is first relaxed using conjugate gradient energy minimization and the relaxed within an NVT (fixed number of particles N , volume V and temperature T) ensemble for 50 ps with non-periodic boundary conditions in all directions at a fixed temperature $T = 4.2 \text{ K}$. The graphene is then stretched by moving the right and left edges at a constant strain rate of $\sim 0.005/\text{ps}$ which is slower than our previous work. In this work, we use a $\text{rcmin_CC} = 1.92 \text{ \AA}$ cutoff for the REBO potential and a 6.8 \AA cutoff for the Lennard-Jones term in the AIREBO potential. Other parameter values in the AIREBO potential are kept the same following the default CH.airebo. The $\text{rcmin_CC} = 1.92 \text{ \AA}$ cutoff is chosen to avoid artificial strain hardening behavior [40, 41]. We use a NVT time damping constant $t_{\text{damp}} = 10$. To calculate the 3D stress we multiply the stress tensor σ_{xx} (along the loading) by the virial thickness (simulation box) and divide it by an effective graphene thickness of 3.35 \AA . Similar procedures have been used for other MD and density functional theory simulations and experiments [7, 34, 42, 43].

Machine Learning

We used TensorFlow (version r1.12) to build the sAE [44]. We used scikit-learn [45] for the principle component analysis (PCA). The TensorFlow r1.12 was run on four CPUs and one NVIDIA Tesla K40m GPU card.

For the encoder, we use a deep neural network (DNN) architecture similar to our previous work [8]. The first part of the DNN consists of three convolutional layers with 16, 32, and 64 filters followed by two fully-connected layers (FCL) of size 512 neurons and 128 neurons. A stride of 1 and a kernel of size 3×3 are used in the convolutional layers. For the decoder, we use two FCLs with 512 and 1024 neurons without convolutional layers. A schematic of the sAE is shown in Fig. 1(a) of the main text. Each convolutional layer is followed by rectified linear unit (ReLU) activation function and max pooling. Each FCL is followed by ReLU activation functions except for the last layer (output layer) of the decoder where we use sigmoid activation functions to generate the reconstructed image (of size 30×80), which is a string of 0s and 1s. This proposed ML network enables us to simultaneously learn to predict the desired multi-target properties while also reconstructing the structures.

Both losses \mathcal{L}^x and \mathcal{L}^y are monitored and the training is stopped when the losses are within the range of desired accuracy. We used the mean square error loss to monitor the loss for the ultimate strain and ultimate stress and used the accuracy score to monitor the performance of the model for reconstruction. The accuracy score is the ratio of the correctly placed elements (holes

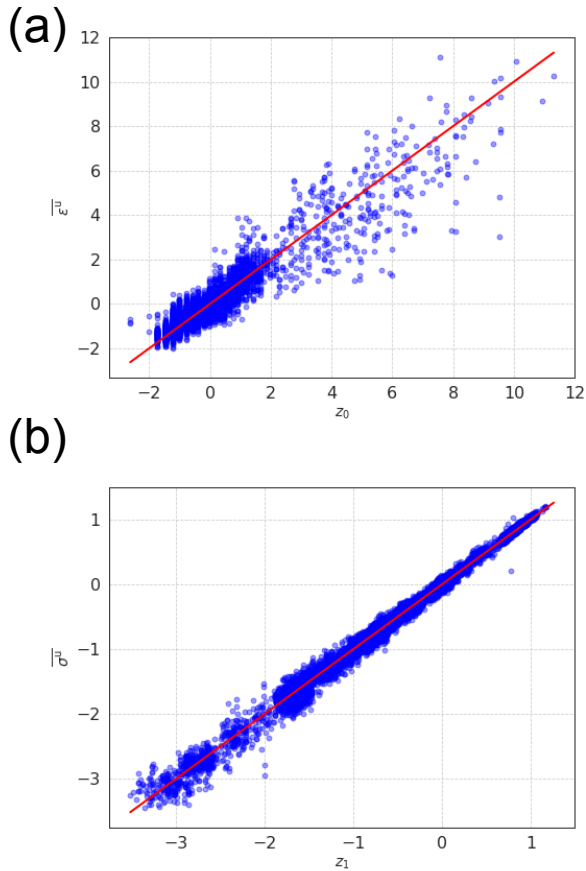


FIG. 6. Plot of true values as a function of predicted values for (a) normalized ultimate strain and (b) normalized ultimate stress (b).

or no holes) divided by the total number of unit graphene cells. Specifically, we stop the training when the \mathcal{L}^y validation loss of σ^u and ϵ^u start increasing and becoming much larger than the training loss—an indication of overfitting—and we ensure that the reconstruction loss \mathcal{L}^x is around 0.001—a tolerance of misplacing three unit cells out of 2400 unit cells. We found that training the sAE for too long (too large a number of epochs) will result in a model with a high reconstruction accuracy but a poor performance for predicting mechanical properties. We thus decided that epoch of 80 represented an appropriate balance between reconstruction and property prediction loss as shown in Fig. 5. In this plot we use sAE with two convolutional layers followed by two fully connected layers of size 512 and 128 (encoder), a latent dimension of size 10, and two fully connected layers of size 512 and 1028 (decoder). In addition, we report R^2 score to attest the performance of property prediction as we did in our previous work [8]. A learning rate of 0.0001 with a batch size of 128 and epoch 80 were used. The Adam optimizer was used for minimizing the total loss.

In Fig. 6, we plot the property predictions of the su-

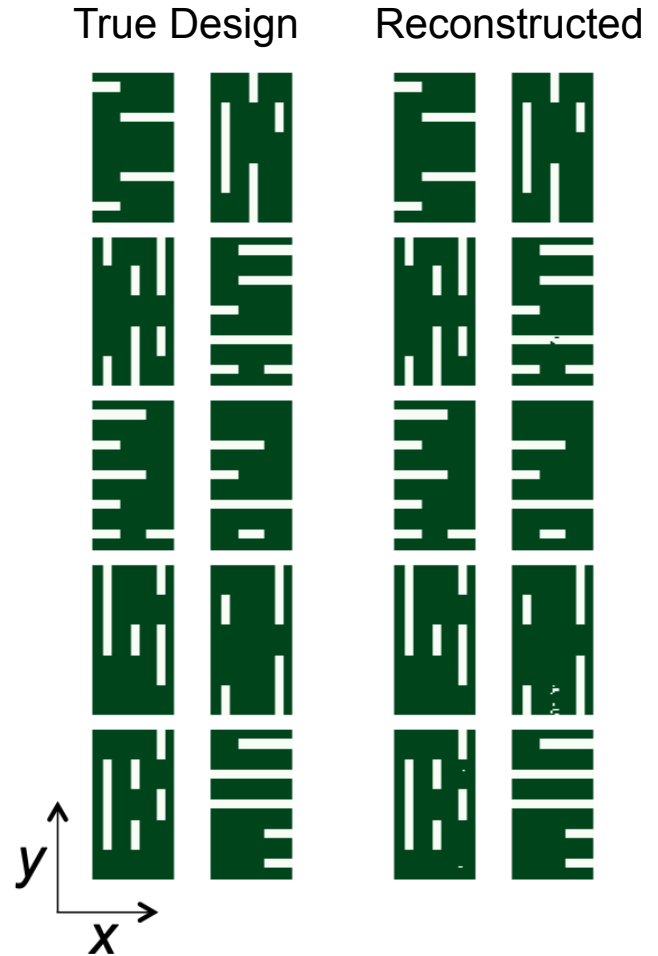


FIG. 7. Reconstructions of inputs obtained from the test set. The sAE can reconstruct the input data closely to the ground truth.

pervised autoencoder (sAE) on the *test* set. The R^2 on the training, validation, and test sets for σ^u (ϵ^u) are 0.99 (0.92), 0.99 (0.87) and 0.99 (0.87), respectively. We see that the sAE can reconstruct the test data (configurations in real space) very close to the ground truth with some imperfections, shown in Fig. 7. We use the fraction of correctly placed graphene unit cell as an accuracy metric and we obtain accuracies of 99.4% for training, validation, and test sets. Note that while the ML has never seen the test set, the test set is taken from a data set that contains either parallel or orthogonal cuts only. As discussed in the main text, we investigate how well the ML can generalize for structures *far* beyond the training samples—such as *mixed* cuts.

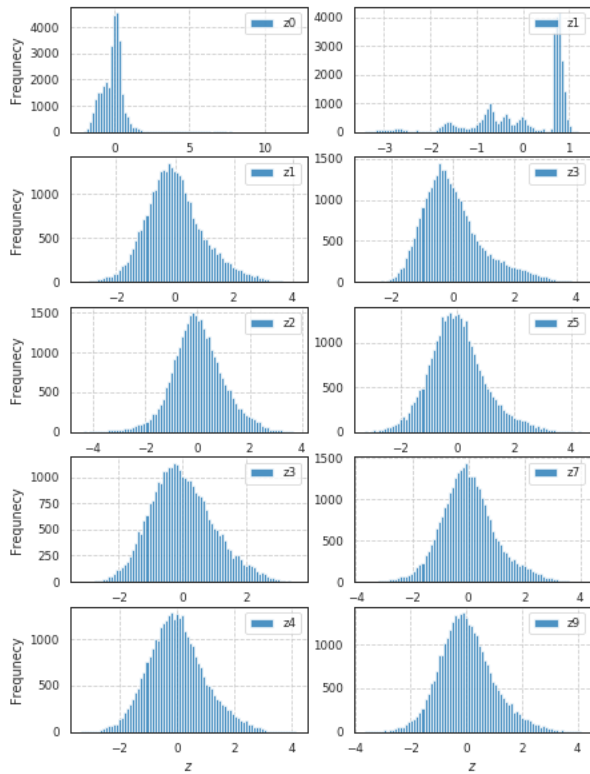


FIG. 8. Histogram of all latent variables (z s) obtained by passing the training data through the encoder.

Latent variable distribution

To find the distribution of latent vectors z we pass the training set through the encoder to obtain the latent vector for each training data point (see Fig. 8). We see that z can have a Gaussian distribution. We find that the sAE can generate non-Gaussian distributions of ϵ^u and σ^u . Fig. 9 shows how the histograms of z_0 and z_1 closely represent the actual values of ϵ^u and σ^u .

Validating SLERP predictions

In a p -dimensional space, we can write $\mathbf{z} = (z_0, z_1, \dots, z_{p-1})$ in terms of a radius r and $p - 1$ angles $(\phi_0, \phi_1, \dots, \phi_{p-2})$.

$$z_0 = r \prod_{k=0}^{p-2} \cos \phi_k \quad (5)$$

$$z_i = r \sin \phi_{i-1} \prod_{k=i}^{p-2} \cos \phi_k, \quad i = 1, \dots, p-2 \quad (6)$$

$$z_{p-1} = r \sin \phi_{p-2} \quad (7)$$

Here we compare the MD simulation results and the prescribed values (via interpolation). We randomly se-

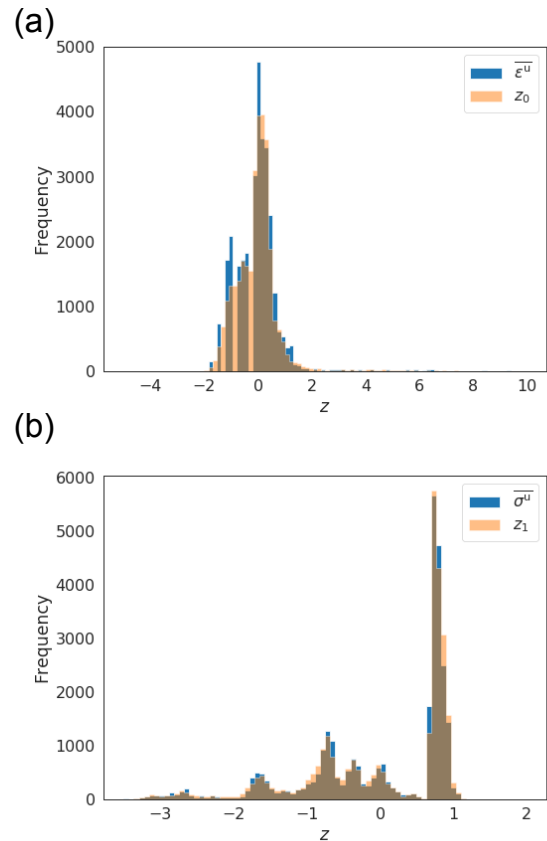


FIG. 9. Histograms of the true values of normalized yield strain $\bar{\epsilon}^y$ and hidden variable z_0 . (b) Histogram of the true values of normalized yield stress $\bar{\sigma}^y$ and hidden variable z_1 . The encoder is trained to predict ϵ^y and σ^y , and indeed finds similar distributions.

lected structures from different domains. Fig. 10 shows the structures generated by interpolation in the latent space. In the first column, the top (bottom) row is the first (second) parent which is randomly selected from the top 1000 designs sorted based on ϵ^u . In the second column parents are selected from the bottom 1000. New designs can be generated smoothly by interpolating two structures that are close in the latent space—i.e. that have similar σ^u and ϵ^u . As shown in Fig. 10, the interpolation scheme allows us to generate similar structures in regions that are close to the training domain.

Next, in the 3rd to 6th rows, for the first column (first parent) configurations are randomly selected from the top 1000 of the training set sorted based on ϵ^u , while in the 7th to 10th rows the first columns configurations are randomly selected from the bottom 1000 sorted based on ϵ^u . For the last column (second parent) in the 3rd to 10th rows, configurations are randomly selected from the entire training set. We use this selection scheme to show how the interpolation scheme performs in different regions.

Next, we compare the ML predictions and the MD

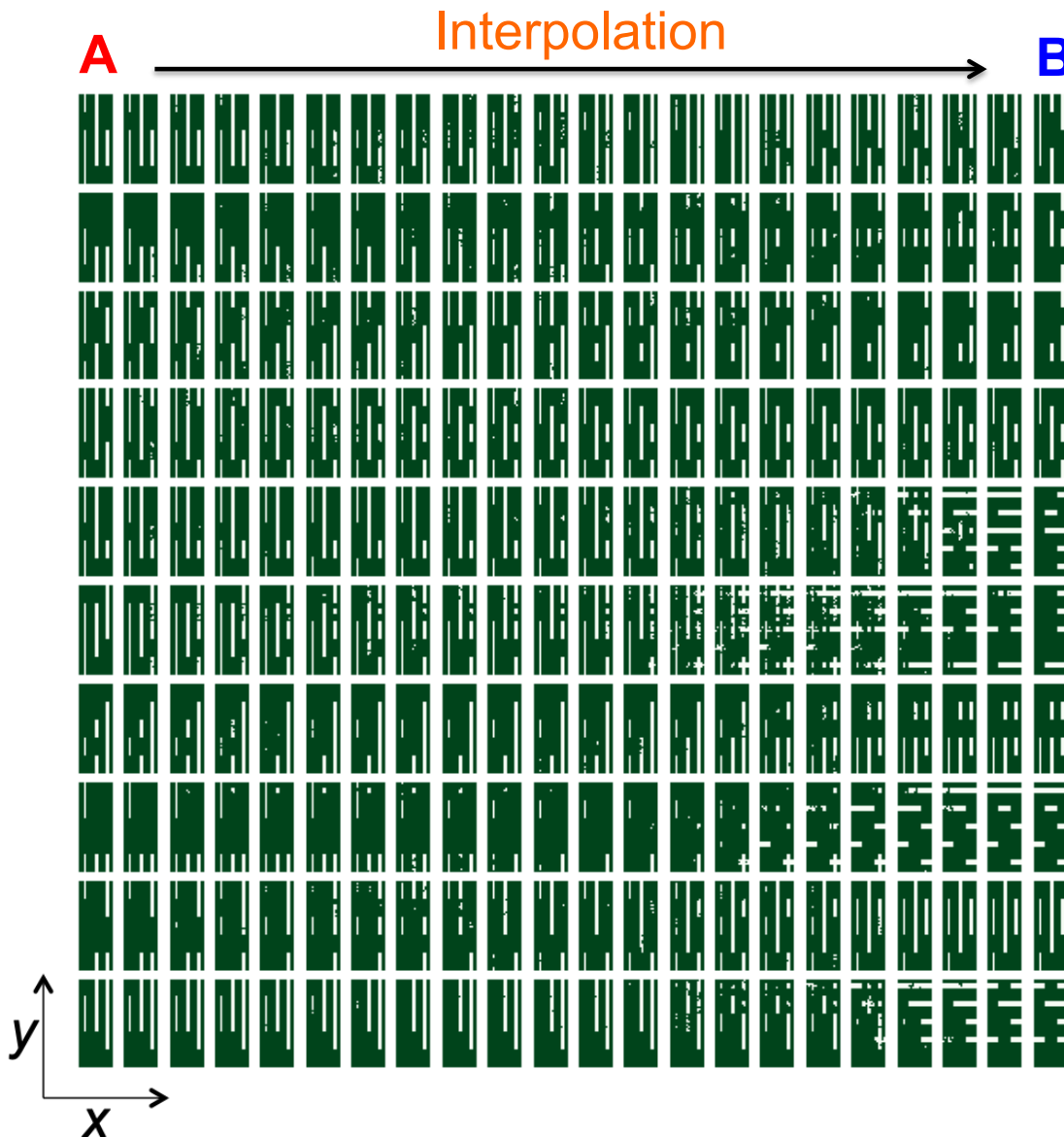


FIG. 10. New designs generated by interpolating from parent A to parent B with 20 steps. Some structures with mixed cuts are obtained when the two parent structures have distinct cut types. Kirigamis are stretched along the x -axis.

results (see Fig. 11 (a) and (b)). For clarity we also plot the histograms of relative error. Relative error is defined as

$$\text{Relative error} = \frac{y_{\text{ML}} - y_{\text{MD}}}{y_{\text{MD}}} \times 100\%, \quad (8)$$

where y_{ML} is the mechanical property predicted by ML and y_{MD} is the mechanical property obtained from MD simulations. Note that here we use the real values to compare the relative error. Fig. 11(c) and (d) show the histogram of relative error of ultimate strain and ultimate stress in real units. We see that the property predictions of roughly 100 structures are within 15% error. Generally, the deviation is highest when the interpolated

structures are at the equidistant point from both parents. We can utilize this to generate new novel designs where the ML model are yet to learn a new domain.

Generating Diverse Designs

In this section we show how we can generate more diverse designs by choosing interpolated structures that are mostly different from their parents, as measured by the angular distance. We selected 100 random configurations from the training set and from this set we obtained 4950 paired parents. We then generated new designs using

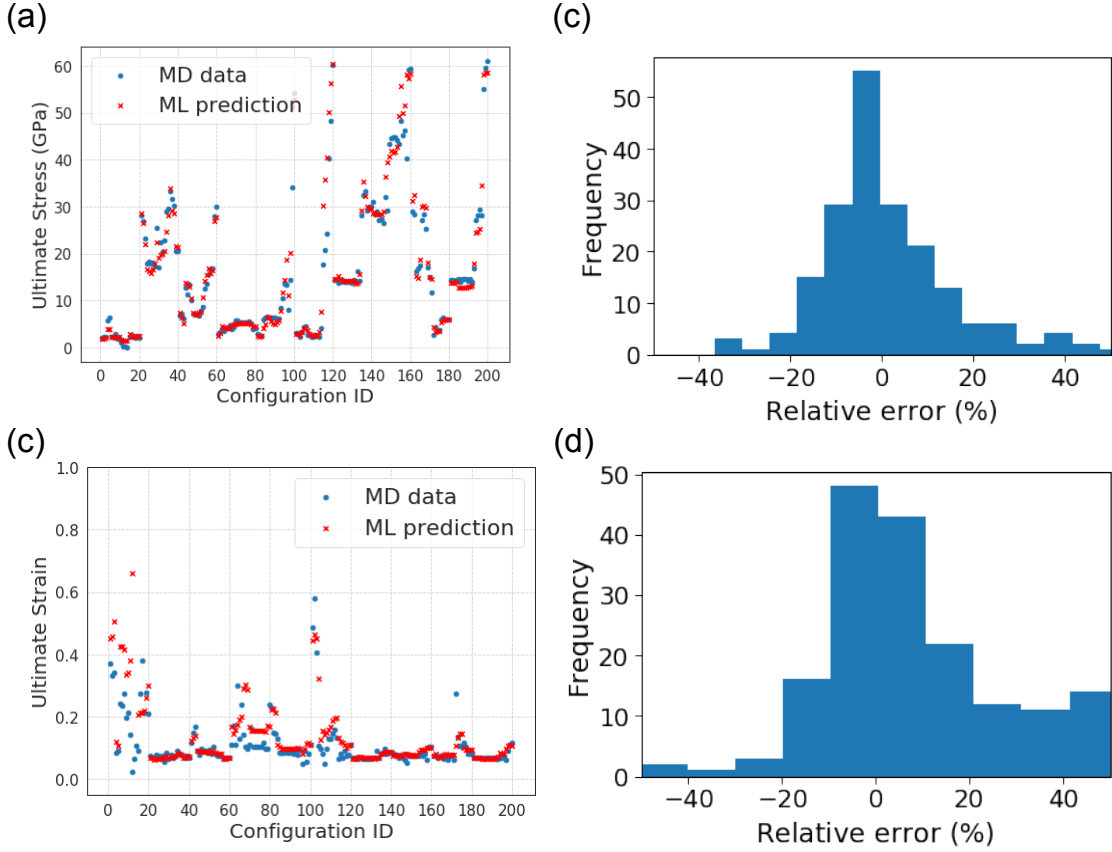


FIG. 11. Comparison between (a) ultimate strain and (b) ultimate stress values of MD results and ML predictions. Configuration ID 1 to 20 are structures with interpolation path 1 and so on. There are 10 paths and each path has 20 interpolation steps; this gives a total of 200 configurations. Histograms of relative errors for (c) ultimate stress and (d) ultimate strain. The corresponding interpolated structures are plotted in Fig. 10.

these 4950 paired parents with 20 interpolation steps. Here we contrast two search strategies. In the first strategy we only select designs with highest strain and in the second strategy we select designs that are the most different from their parents, as measured by the angular distance. For easier comparison, we selected 200 representative configurations (out of 4950) with $\bar{\epsilon}^u > 1$ and $\bar{\sigma}^u > -3$. In Fig. 12, we can see that there are many structures with mixed and overlapping cuts where the strategy to achieve maximum structural difference was used. On the other hand using the first strategy (maximizing strain only), we obtained only two structures containing mixed cuts, as shown in Fig. 13. To conclude, we can use our ML model and the angular distance metric to generate structures that are different from the training set.

* paul.hanakata@gmail.com

[1] M. A. Dias, M. P. McCarron, D. Rayneau-Kirkhope, P. Z. Hanakata, D. K. Campbell, H. S. Park, and D. P.

Holmes, *Soft matter* **13**, 9087 (2017).
 [2] A. Rafsanjani and K. Bertoldi, *Phys. Rev. Lett.* **118**, 084301 (2017).
 [3] Y. Yang, M. A. Dias, and D. P. Holmes, *Physical Review Materials* **2**, 110601 (2018).
 [4] M. Moshe, E. Esposito, S. Shankar, B. Bircan, I. Cohen, D. R. Nelson, and M. J. Bowick, *Physical review letters* **122**, 048001 (2019).
 [5] T. C. Shyu, P. F. Damasceno, P. M. Dodd, A. Lamoureux, L. Xu, M. Shlian, M. Shtein, S. C. Glotzer, and N. A. Kotov, *Nature materials* **14**, 785 (2015).
 [6] M. K. Bles, A. W. Barnard, P. A. Rose, S. P. Roberts, K. L. McGill, P. Y. Huang, A. R. Ruyack, J. W. Kevek, B. Kobrin, D. A. Muller, *et al.*, *Nature* **524**, 204 (2015).
 [7] P. Z. Hanakata, Z. Qi, D. K. Campbell, and H. S. Park, *Nanoscale* **8**, 458 (2016).
 [8] P. Z. Hanakata, E. D. Cubuk, D. K. Campbell, and H. S. Park, *Physical review letters* **121**, 255304 (2018).
 [9] Y. Tang and J. Yin, *Extreme Mechanics Letters* **12**, 77 (2017).
 [10] A. Rafsanjani, Y. Zhang, B. Liu, S. M. Rubinstein, and K. Bertoldi, *Science Robotics* **3**, eaar7555 (2018).
 [11] A. Seko, A. Togo, H. Hayashi, K. Tsuda, L. Chaput, and I. Tanaka, *Physical review letters* **115**, 205901 (2015).

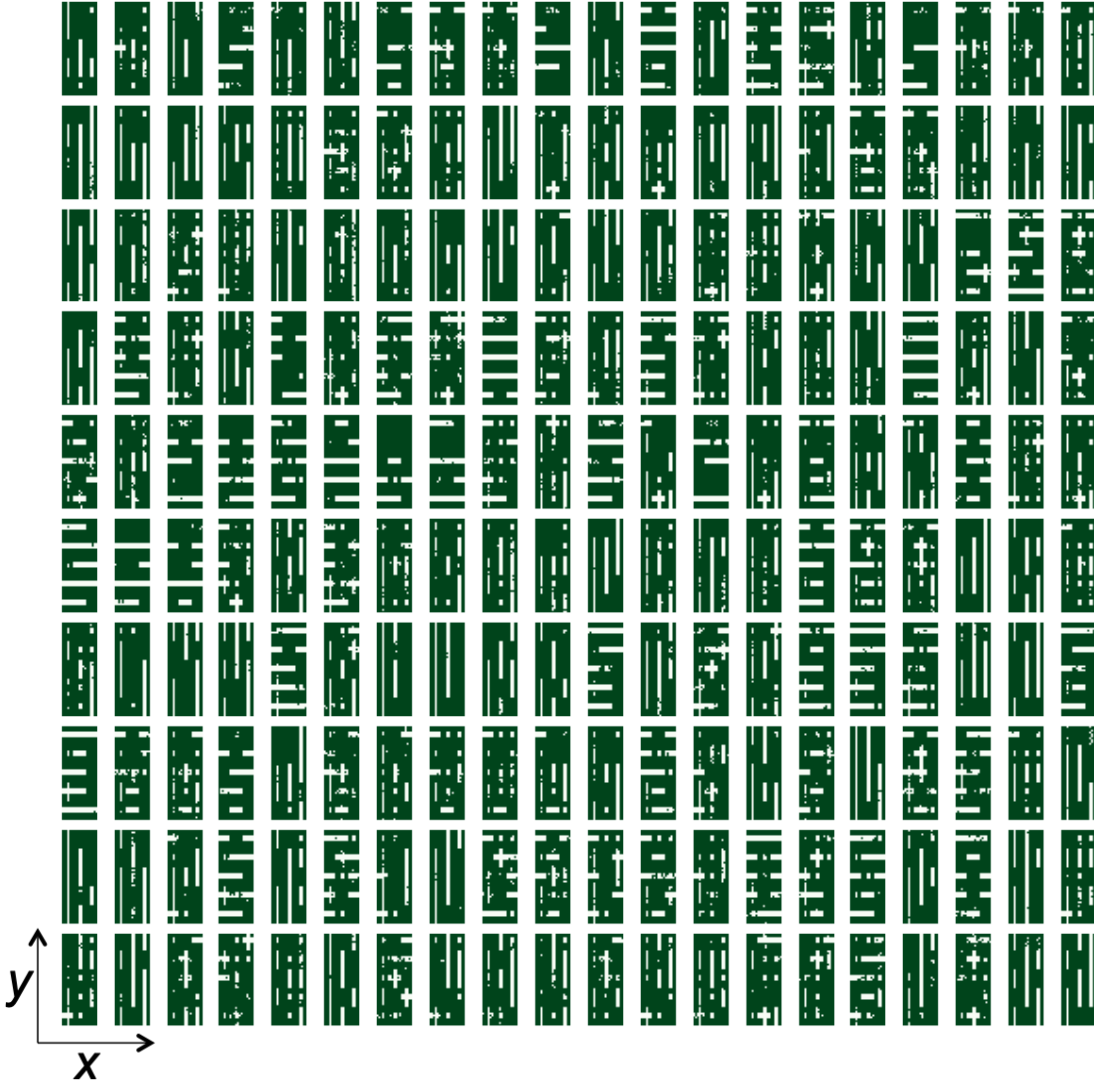


FIG. 12. Generated structures by maximizing diversity. Kirigamis are stretched along the x -axis. The relative errors are plotted in Fig. 14 (a) and (b).

- [12] G. X. Gu, C.-T. Chen, and M. J. Buehler, *Extreme Mechanics Letters* **18**, 19 (2018).
- [13] D. P. Kingma and M. Welling, *arXiv preprint arXiv:1312.6114* (2013).
- [14] K. Kim, S. Kang, J. Yoo, Y. Kwon, Y. Nam, D. Lee, I. Kim, Y.-S. Choi, Y. Jung, S. Kim, *et al.*, *npj Computational Materials* **4**, 67 (2018).
- [15] R. Gómez-Bombarelli, J. N. Wei, D. Duvenaud, J. M. Hernández-Lobato, B. Sánchez-Lengeling, D. Sheberla, J. Aguilera-Iparraguirre, T. D. Hirzel, R. P. Adams, and A. Aspuru-Guzik, *ACS central science* **4**, 268 (2018).
- [16] J. Noh, J. Kim, H. S. Stein, B. Sanchez-Lengeling, J. M. Gregoire, A. Aspuru-Guzik, and Y. Jung, *Matter* **1**, 1370 (2019).
- [17] W. Ma, F. Cheng, Y. Xu, Q. Wen, and Y. Liu, *Advanced Materials* **31**, 1901111 (2019).
- [18] To normalize \mathbf{y} , we first take the log of ϵ^u and σ^u , then subtract from each value its mean, then divide it by its standard deviation. We normalize these two quantities so that they lie within a similar range.
- [19] M. Shanker, M. Y. Hu, and M. S. Hung, *Omega* **24**, 385 (1996).
- [20] P. Mehta, M. Bukov, C.-H. Wang, A. G. Day, C. Richardson, C. K. Fisher, and D. J. Schwab, *Physics reports* (2019).
- [21] The maximum cut density of parallel cuts are 15 as there are not detached structures.
- [22] LAMMPS, <http://lammps.sandia.gov> (2012).
- [23] M. Moshe, E. Esposito, S. Shankar, B. Bircan, I. Cohen, D. R. Nelson, and M. J. Bowick, *Physical Review E* **99**, 013002 (2019).
- [24] B. Zheng and G. X. Gu, *Carbon* **155**, 697 (2019).
- [25] S. J. Wetzel, *Physical Review E* **96**, 022140 (2017).
- [26] T. White, *arXiv preprint arXiv:1609.04468* (2016).
- [27] D. Ha and D. Eck, *arXiv preprint arXiv:1704.03477* (2017).

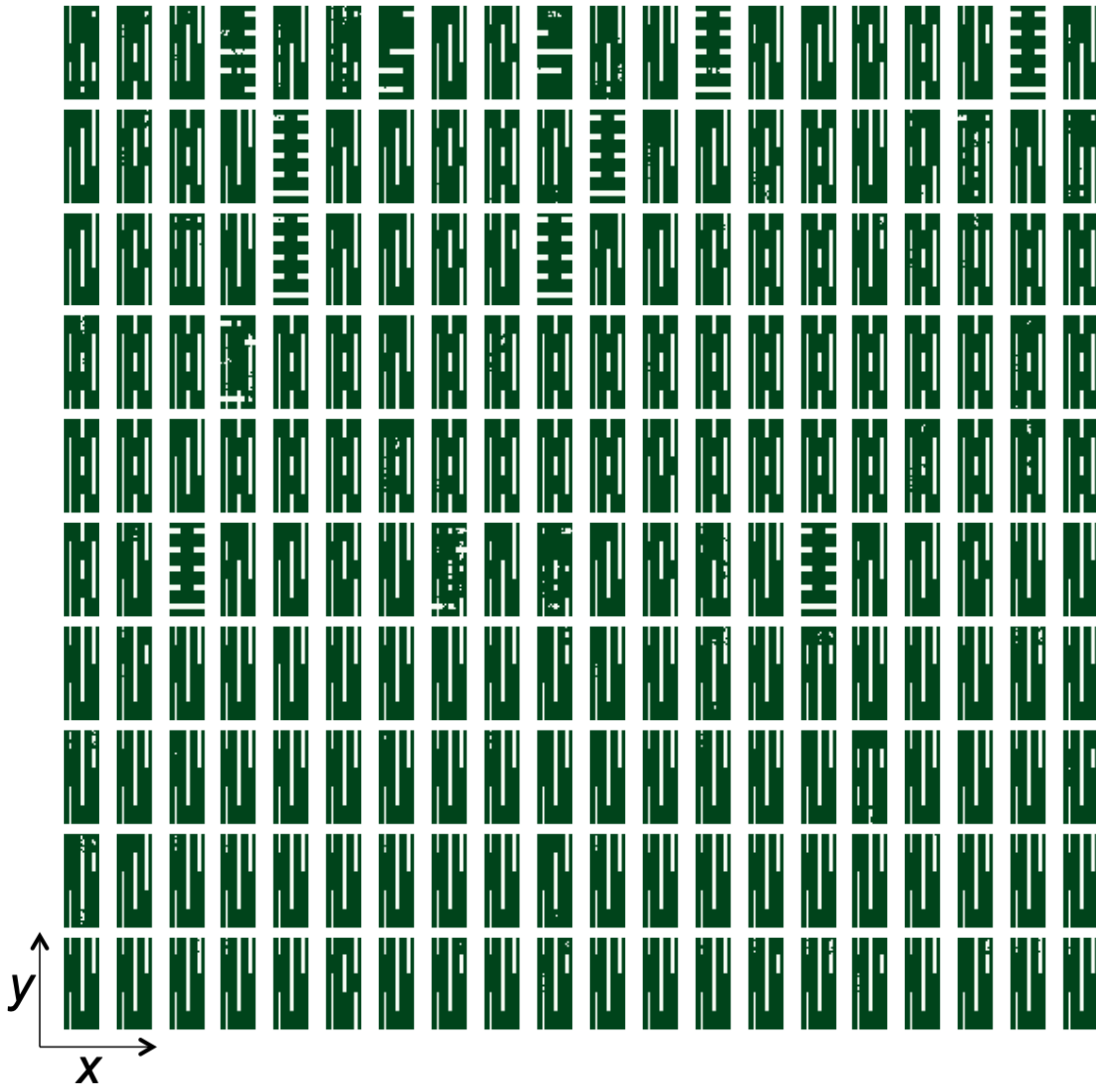


FIG. 13. Generated structures by maximizing strain. Kirigamis are stretched along the x -axis. The relative errors are plotted in Fig. 14(c) and (d).

- [28] C. Szegedy, W. Zaremba, I. Sutskever, J. Bruna, D. Erhan, I. Goodfellow, and R. Fergus, arXiv preprint arXiv:1312.6199 (2013).
- [29] S. Dodge and L. Karam, in *2017 26th international conference on computer communication and networks (ICCCN)* (IEEE, 2017) pp. 1–7.
- [30] N. Ford, J. Gilmer, N. Carlini, and D. Cubuk, arXiv preprint arXiv:1901.10513 (2019).
- [31] One example is that two equivalent structures by reflection symmetries (have same mechanical properties) will be identified as two different structures by Tanimoto distance metric; on the other hand the angular distance metric will measure how two designs are different structurally and mechanically.
- [32] E. Lejeune, *Extreme Mechanics Letters*, 100659 (2020).
- [33] Z. Qi, D. K. Campbell, and H. S. Park, *Phys. Rev. B* **90**, 245437 (2014).
- [34] P. Z. Hanakata, A. Carvalho, D. K. Campbell, and H. S. Park, *Physical Review B* **94**, 035304 (2016).
- [35] P. Z. Hanakata, A. S. Rodin, A. Carvalho, H. S. Park, D. K. Campbell, and A. H. Castro Neto, *Physical Review B* **96**, 161401 (2017).
- [36] H. Rostami, F. Guinea, M. Polini, and R. Roldán, *npj 2D Materials and Applications* **2**, 15 (2018).
- [37] P. Z. Hanakata, A. Rodin, H. S. Park, D. K. Campbell, and A. C. Neto, *Physical Review B* **97**, 235312 (2018).
- [38] V. Torres, P. Silva, E. de Souza, L. Silva, and D. Bahamon, *Physical Review B* **100**, 205411 (2019).
- [39] S. J. Stuart, A. B. Tutein, and J. A. Harrison, *The Journal of chemical physics* **112**, 6472 (2000).
- [40] Y. Wei, J. Wu, H. Yin, X. Shi, R. Yang, and M. Dresselhaus, *Nature materials* **11**, 759 (2012).
- [41] P. Z. Hanakata, E. D. Cubuk, D. K. Campbell, and H. S. Park, *Phys. Rev. Lett.* **123**, 069901 (2019).

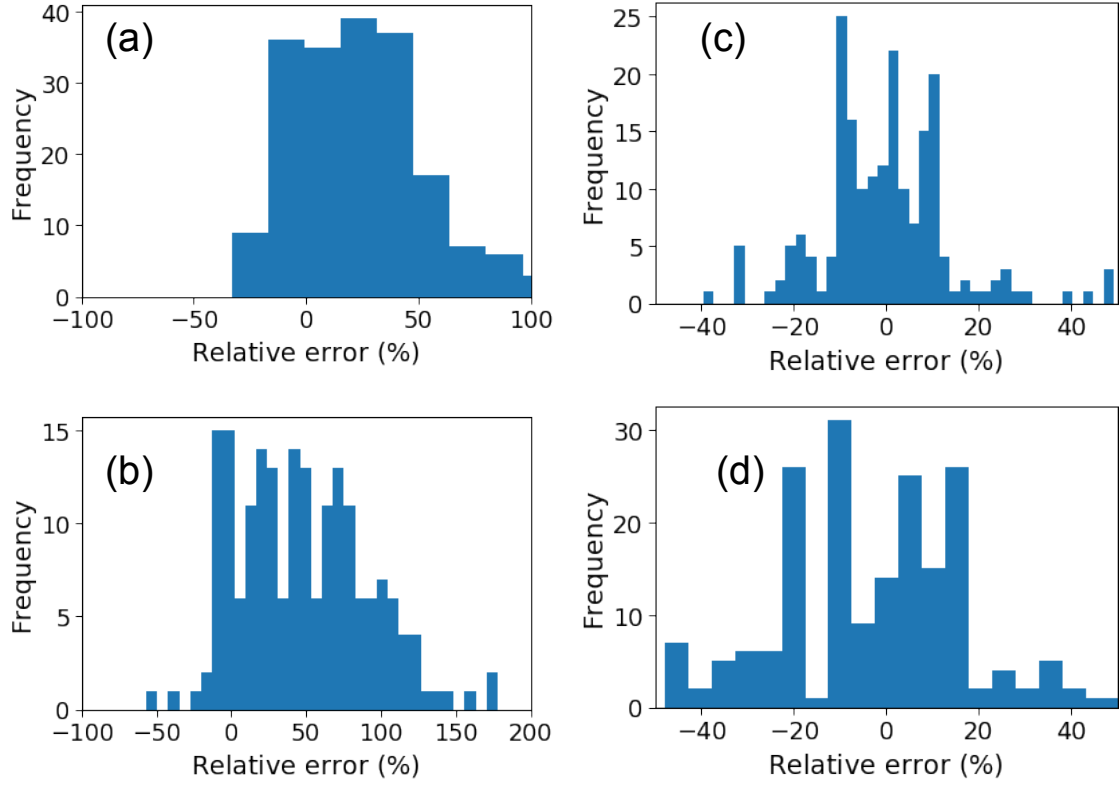


FIG. 14. Histograms of relative errors for (a) ultimate stress and (b) ultimate strain for generated structures with maximizing diversity strategy. Histograms of relative errors for (c) ultimate stress and (d) ultimate strain for generated structures with maximizing strain strategy.

- [42] P. Zhang, L. Ma, F. Fan, Z. Zeng, C. Peng, P. E. Loya, Z. Liu, Y. Gong, J. Zhang, X. Zhang, *et al.*, *Nature communications* **5**, 3782 (2014).
- [43] C. Lee, X. Wei, J. W. Kysar, and J. Hone, *science* **321**, 385 (2008).
- [44] M. Abadi, A. Agarwal, P. Barham, E. Brevdo, Z. Chen, C. Citro, G. S. Corrado, A. Davis, J. Dean, M. Devin, S. Ghemawat, I. Goodfellow, A. Harp, G. Irving, M. Isard, Y. Jia, R. Jozefowicz, L. Kaiser, M. Kudlur, J. Levenberg, D. Mané, R. Monga, S. Moore, D. Murray, C. Olah, M. Schuster, J. Shlens, B. Steiner, I. Sutskever, K. Talwar, P. Tucker, V. Vanhoucke, V. Vasudevan, F. Viégas, O. Vinyals, P. Warden, M. Wattenberg, M. Wicke, Y. Yu, and X. Zheng, “**TensorFlow: Large-scale machine learning on heterogeneous systems,**” (2015), software available from tensorflow.org.
- [45] F. Pedregosa, G. Varoquaux, A. Gramfort, V. Michel, B. Thirion, O. Grisel, M. Blondel, P. Prettenhofer, R. Weiss, V. Dubourg, J. Vanderplas, A. Passos, D. Cournapeau, M. Brucher, M. Perrot, and E. Duchesnay, *Journal of Machine Learning Research* **12**, 2825 (2011).